Mechanical properties of $BaCe_{0.65}Zr_{0.2}Y_{0.15}O_{3-\delta}$ – $Ce_{0.85}Gd_{0.15}O_{2-\delta}$ dual-phase proton-conducting material with emphasis on micro-pillar splitting

Wenyu Zhou[1,2,*], Jürgen Malzbender[1], Fanlin Zeng[1], Wendelin Deibert[1], Louis Winnubst[2], Arian Nijmeijer[2], Olivier Guillon[1], Ruth Schwaiger[1,3], Wilhelm Albert Meulenberg[1,2]

[1] Forschungszentrum Jülich GmbH, Institute of Energy and Climate Research (IEK), 52425 Jülich, Germany

[2] University of Twente, Faculty of Science and Technology, Inorganic Membranes, P.O. Box 217, 7500 AE, Enschede, the Netherlands

[3] Chair of Energy Engineering Materials, RWTH Aachen University, 52056 Aachen, Germany

Abstract

$BaCe_{0.65}Zr_{0.2}Y_{0.15}O_{3-\delta}$ – $Ce_{0.85}Gd_{0.15}O_{2-\delta}$ (BCZ20Y15-GDC15) dual-phase material revealed potential for H_2 production technologies due to its exceptional H_2 permeation and chemical resistance. In this article, mechanical properties of BCZ20Y15-GDC15 dual-phase material were investigated to evaluate the mechanical behavior and develop strategies to warrant structural stability. Elastic modulus, hardness and fracture toughness values were studied using different indentation-based methods. The fracture experiments at different length-scales both revealed that the introduction of GDC15 makes the material tougher, facilitating the further design of robust and reliable components.

Keywords: Dual-phase, proton conductor, mechanical properties, indentation, micro-pillar splitting, fracture toughness

*Corresponding author
Email: w.zhou@fz-juelich.de, Tel.: ++49-2461-619399, Fax: ++49-2461-612455

1. Introduction

$BaCeO_3$-based protonic conductor materials [1-6] revealed the highest reported proton conductivities, in particular when doped with 15% Y [7, 8]. Furthermore, doping levels exceeding 20% Zr enhance the chemical stability against CO_2, H_2O and H_2S [9-13]. However, the poor electronic conductivity of BCZ20Y15 limits the ambipolar conductivity, thus reducing or even precluding the H_2 permeation across the membrane [13-15]. Although further doping with metals of variable oxidation states on the B-site of the ABO_3 perovskite (BCZ20Y15) could be a strategy to enhance the electronic conductivity but this could be detrimental to the protonic transport depending on the dopant [16]. The introduction of an electronic conducting secondary phase forming a dual-phase composite [17] represents another promising option. In this context, ceramic-metal (cer-met) composite membranes have been successfully investigated [18-23]. All-ceramic (ceramic-ceramic) systems have already demonstrated significant advantages regarding mechanical and chemical stabilities [24-31].

Studies on all-ceramic $BaCe_{0.65}Zr_{0.2}Y_{0.15}O_{3-\delta} - Ce_{0.85}Gd_{0.15}O_{2-\delta}$ (BCZ20Y15-GDC15) have revealed its exceptional hydrogen permeation [17], enhanced sulfur tolerance [32], good chemical stability in moist CO_2 environments [17, 32] and structural stability [33, 34] and indicate its potential for the technological application.

Despite the progress with respect to conductivity and chemical stability, only few studies have focused on the mechanical properties of all-ceramic dual phase gas transport membranes [35-41]. To the best of our knowledge, no systematic investigation conducted to understand the mechanical properties of BCZ20Y15-GDC15.

Elastic modulus and hardness can be determined using indentation testing [42-44], while the validity of conventional indentation testing-based fracture toughness investigations is still under discussion [45]. Recently, Sebastiani et al. [46-49] developed fracture toughness assessment based

on a micro-pillar indentation splitting test based on sharp indentations into micro-pillars prepared via focused ion beam (FIB) milling. The pillar splitting method was developed with the aim of characterizing microscale intrinsic fracture toughness on the basis of critical load values visible as kink effects [47] in the load-depth curves acquired during the pillar indentation process. Compared to the conventional Vickers-indentation-based fracture toughness test method (VIF) and other currently available microscale mechanical testing methods, e.g., single and double cantilever testing [46], the micro-pillar test method offers several advantages, including its ease of application. Post-test measurement of the crack length, a factor that is critical for the VIF method and highly dependent on the imaging characteristics, is not necessary for the micro-pillar test method [47, 50]. Furthermore, potential residual stress, which might be induced by stoichiometric gradients or differences in thermal expansion in the case of a thin film on a substrate, is fully released and does not affect the test if the pillars have an aspect ratio of height to diameter between 1 and 4 [51]. Difficulties related to friction coefficient calibration and possible Ga^+ ion implantation at the root of the stress-concentrating notch, which complicate the analysis of microcantilever fracture experiments, can be avoided [46, 47]. However, also in the case of pillar-splitting, size effects were observed, which were related to the FIB-preparation [51, 52]. While it is not necessary to determine the crack length, the validity of every splitting experiment needs to be confirmed since inaccuracies in the indenter tip positioning can result in an underestimation of the fracture toughness [51].

In this work, the mechanical properties of dual-phase BCZ20Y15-GDC15 were investigated. The study involved indentation testing at different length scales, yielding elastic modulus and hardness values. Furthermore, micro-pillar splitting tests were performed. A detailed microstructural analysis revealed the mechanism responsible for the toughening effect of GDC15.

2. Experimental

BCZ20Y15-GDC15 samples were prepared by a solid state reaction method (SSR). $BaCO_3$ (99%, Sigma Aldrich), CeO_2 (99.9%, Sigma Aldrich), ZrO_2 (99%, Sigma Aldrich), Y_2O_3 (99%, Sigma Aldrich), and Gd_2O_3 (99%, Sigma Aldrich) were used as starting materials. In the process, BCZ20Y15 and GDC15 were prepared separately. Precursor powders were mixed according to the stoichiometry and ball-milled (Rollermill RM1, Zoz GmbH, Wenden, Germany. ZrO_2 balls, 3.5 mm diameter, weight ratio powder : balls : ethanol = 1 : 2 : 3) in ethanol for 24 h. The resultant mixtures were dried at 80 °C for two to three days. Then, the BCZ20Y15 mixtures were calcined at 1300 °C for 5 h, and the GDC15 mixtures at 1200 °C for 12 h [52, 53]. Afterwards, the two compositions were mixed (shaker mixer TURBULA T2, Willy A. Bachofen GmbH, Nidderau, Germany) in a 50 : 50 volume ratio, with additional 0.5 wt. % (of BCZ20Y15 weight) NiO (99%, Sigma Aldrich) [17] as sintering aid in order to obtain dense samples. In order to obtain powders with a fine and homogeneous grain size, pre-calcined mixture powders were ball-milled in ethanol for 24 h. Finally, the powder mixtures were dried and sieved through a 160 μm mesh.

Bulk membranes were uniaxially pressed into a disc shape under a pressure of ~ 20 MPa for 5 minutes to obtain green samples with diameter and thickness of ~ 27 mm and ~ 1 mm, respectively. The samples were subsequently sintered at 1500 °C for 5 hours in air using a constant heating / cooling rate of 5 $K \cdot min^{-1}$.

The crystal structure and phase purity of the sintered samples was characterized using an EMPYREAN (PANalytical) diffractometer with parafocusing Bragg-Brentano geometry, employing a Cu-LFF-tube (40 kV / 40 mA), a BBHD mirror (Bragg-BrentanoHD mirror, manufactured by Malvern Panalytical, Ltd., Malvern, UK), 0.04 rad Soller slits, and a PIXcel3D detector. X-ray diffraction (XRD) patterns were recorded at room temperature using a step scan procedure (0.4 s per step, 0.013 ° per step size) in the 2θ range of 5 – 90 °.

The microstructures and topographies of the samples were assessed by a Zeiss SUPRA 50VP field emission scanning electron microscope (SEM, Zeiss Microscopy GmbH, Oberkochen, Germany). The respective specimen was first embedded in epoxy resin, ground sequentially using SiO_2 sandpaper with 400 and 2000 grit size and then polished using 6 µm and 1 µm diamond suspension. The final polishing was conducted using 50 nm colloidal silica polishing suspension. The image analysis software Image J [54] was used to determine the grain size and porosity from the electron backscatter diffraction (EBSD, HKL Nordlys model, Oxford Instruments, High Wycombe, UK.) phase mapping. Energy dispersive X-ray (EDX) spectroscopy was carried out at 10 kV accelerating voltage using a X-Max 80 detector and the AZtec data acquisition and analysis software package (Oxford Instruments Nanoanalysis, High Wycombe, United Kingdom).

Depth-sensing indentation testing was carried out using an indentation system (MicroMaterials, Ltd., Wrexham, UK), equipped with a diamond Berkovich tip. Elastic modulus and hardness were determined from the load-depth curves under load control following the procedure developed by Oliver and Pharr [55, 56]. The reduced modulus (E_r) was calculated using:

$$E_r = \frac{\sqrt{\pi} \cdot S}{2 \cdot \beta \cdot \sqrt{A_p(h_c)}} \tag{1}$$

where S is the contact stiffness determined from the unloading slope, β a tip-dependent geometry factor assumed as 1.034 , A_p the projected contact area, and h_c the contact depth at the maximum load P_{max}. The plane strain modulus (E^*) then corresponds to:

$$E^* = \frac{1}{\frac{1}{E_r} - \frac{1-\nu_i^2}{E_i}} \tag{2}$$

where E_i is the elastic modulus and ν_i Poisson's ratio of the diamond indenter tip assuming 1141 GPa and 0.07, respectively. Young's modulus E_{IT} was then calculated from E^* using a Poisson's ratio of the sample of $\nu_s = 0.3$, which is typical of ceramics [57]:

$$E_{IT} = E^* \cdot (1 - \nu_s^2) \tag{3}$$

The hardness H_{IT} was determined from the maximum load and the corresponding contact area:

$$H_{IT} = \frac{P_{max}}{A_p} \tag{4}$$

The indentation experiments were conducted to different maximum loads of 20, 200 mN, 1 N and 2 N. Thirty indents at each load were performed at a loading rate of 2 mN/s. The distances between indents were 15 µm and 90 µm at 20 mN and 200 mN, respectively. For higher loads of 1 N and 2 N, the distances between indents were 150 µm and 210 µm, respectively.

The fracture toughness evaluated using the conventional Vickers-indentation-based fracture toughness method [58] at applied loads of 3 N, 5 N and 10 N. Crack length induced by the Vickers indentation was measured immediately after the test to avoid subcritical crack growth effects [59]. The following empirical equation, which was developed for the half-penny crack mode, was used to calculate the apparent fracture toughness K_{IC} [60, 61]:

$$K_{IC} = 0.016 \left(\frac{E}{H}\right)^{\frac{1}{2}} \left(\frac{P}{c^{3/2}}\right) \tag{5}$$

where c is the crack length determined from micrographs, E and H derived from indentation were used.

For the micropillar-based fracture toughness characterization, 8 pillars with nominal diameters of 15 µm were FIB-milled using an Auriga Crossbeam workstation (Zeiss Microscopy GmbH, Oberkochen,

Germany) operated at 30 kV and 4 nA. Table 1 summarizes the actual (real) pillar diameters, which were used for the subsequent evaluation of the fracture toughness values.

Table 1. Nominal and actual pillar diameters.

	Pillar No./Real diameter [µm]							
Nominal diameter [µm]	P1	P2	P3	P4	P5	P6	P7	P8
15	15.9	16.2	16.7	15.1	14.9	16.1	15.9	15.4

The load was applied at a loading rating of 2.5 mN/s and kinks indicate the pillar splitting. The fracture toughness values were then calculated from the kink loads using the following equation [47]:

$$K_{IC} = \gamma \cdot \frac{P_c}{R^{3/2}} \tag{6}$$

where P_c is the critical load at kink, γ is a dimensionless coefficient that includes the influence of elastic-plastic properties and R is the radius of the pillar. The coefficient γ (eq. 6) was initially calculated by means of the finite element method [47], while in later works a linear relationship between γ and E / H was derived, which holds as long as $7 \leq E / H \leq 21$ [62, 63]:

$$\gamma = 0.0149 \frac{E}{H} + 0.057 \tag{7}$$

Using this equation along with the experimentally determined indentation elastic modulus and hardness, γ thus a value of ~ 0.33.

3. Results and discussion

The dual-phase material's crystal structure was verified by XRD (see Fig. 1).

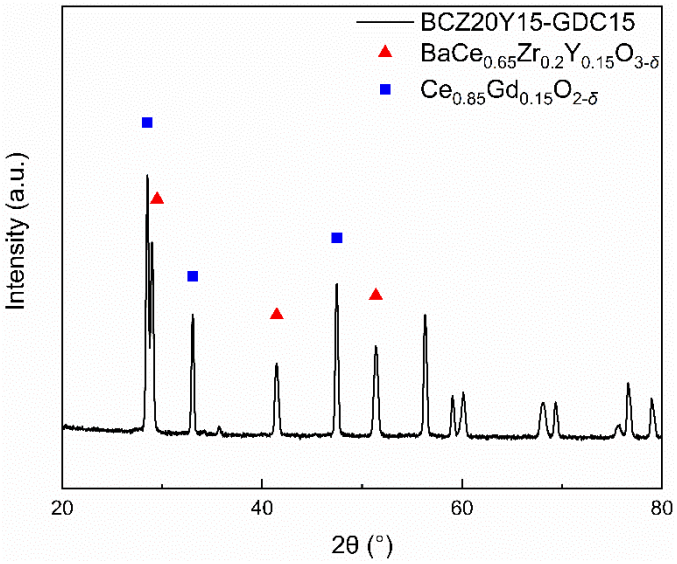

Figure 1. XRD pattern of BCZ20Y15-GDC15, identified according to ICSD 90052 and ICSD 28795. The three strongest peaks corresponding to BCZ20Y15 and GDC15 are marked by the red triangles and the blue squares, respectively. There is no indication of the presence of a 3rd phase.

No third phase was observed in the XRD results, indicating that with 0.5 wt% NiO as sintering aid, after 1500 °C / 5 h sintering, the sample contained only BCZ20Y15 (identified according to ICSD 90052) and GDC15 (identified according to ICSD 28795). From the XRD pattern, no peaks corresponding to NiO can be observed, due to the very low amount of NiO, similar as reported in [52]. The detected room temperature orthorhombic and cubic crystal structures of BCZ20Y15 and GDC15 are in agreement with those reported in [17, 32, 33].

The dual-phase material's microstructure was characterized using SEM (see Fig. 2).

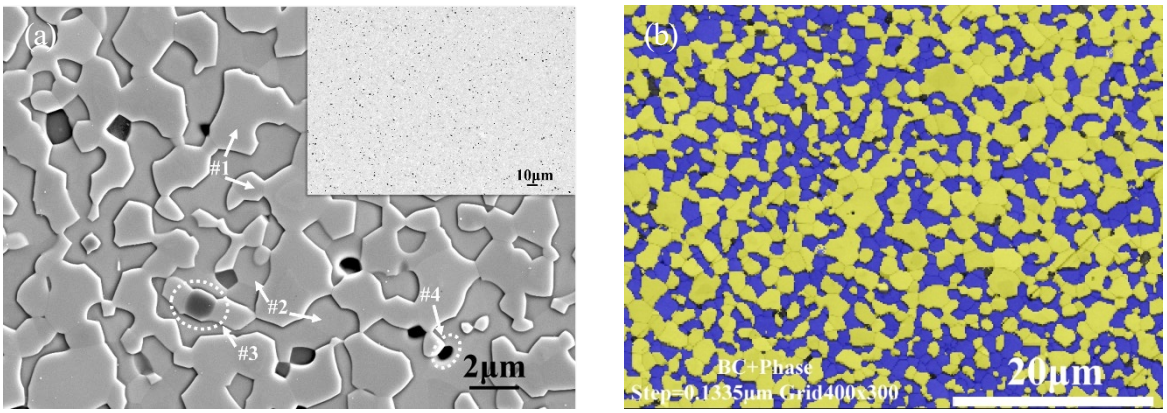

Figure 2. (a) SEM images of BCZ20Y15-GDC15. The black spots in the inset are pores, corresponding to less than 2% of the surface area. The topographically higher (#1) and lower phase (#2) are GDC15 and BCZ20Y15, respectively. Local Ni enrichment (#3) within GDC15 was observed (see Fig. S1). Pores (#4) with typical round shape. (b) EBSD phase mapping combined with band contrast. The yellow areas correspond to GDC15, the blue to BCZ20Y15, with area ratios of ~ 60% and 40%, respectively.

The SEM micrographs indicate a porosity of less than 2% (using Image J [54]). The topographically (Fig. 2 (a)) clearly elevated phase (Fig. 2 (a) #1) and lowered phase (Fig. 2 (a) #2) were observed, corresponding to GDC15 and BCZ20Y15, respectively, as confirmed by EDX and EBSD. Such variation of the topography in a dual-phase ceramic material was also reported in [35, 64], which was explained by large hardness differences of the individual phases.

Local Ni enrichment (Fig. 2 (a) #3) was observed inside the GDC15 phase, similar as reported in [65], indicating that there is no reaction or solubility of Ni and GDC15 [65]. After ball-mixing, NiO exists in the mixture powder. During sintering a small amount of NiO was trapped inside the GDC15, thus not affecting the GDC15 phase sintering process. However, it could not be detected by XRD due to its limited quantity. The observed pores having a round shape (Fig. 2 (a) #4) are similar to those reported in [36, 52, 66-68].

From the EBSD phase mapping combined with band contrast (Fig. 2 (b)), the distribution of two individual phases can be observed. Their actual area ratio (GDC15 - yellow : BCZ20Y15 -

blue) is ~ 60:40 Vol. %. For the sake of clarity, in the further discussion, the materials will be termed with the nominal phase ratio. Individual phases' connection, which is extremely important in dual-phase ceramics and has been discussed in detail in [69-71], appears to have been achieved for both phases. The EBSD analysis also yielded the grain sizes, being for both BCZ20Y15 and GDC15 ~ 1 μm. Considering the authors' previous work on single phase BCZ20Y15 [52], whose grain size is ~ 13 μm, it seems that GDC15 limits the grain growth of BCZ20Y15.

The elastic modulus and hardness values of BCZ20Y15-GDC15 are summarized in Table 2.

Table 2. Elastic modulus and hardness of BCZ20Y15-GDC15.

Load [mN]	20	200	1000	2000
Elastic modulus [GPa]	166 ± 17	163 ± 9	168 ± 10	164 ± 10
Hardness [GPa]	8.5 ± 1.1	9.3 ± 0.7	7.8 ± 0.4	7.2 ± 0.4

Both elastic modulus and hardness determined from the indentation tests are independent of the applied loads, as shown in the Table 2. At loads of 20 and 200 mN, the elastic modulus and the hardness are higher than those determined for single phase BCZ20Y15 (~ 120 GPa and ~ 7 GPa) [52], at the same applied loads. This indicates that after introduction of GDC15 into the material, forming the dual-phase BCZ20Y15-GDC15, both the apparent elastic and plastic properties are enhanced. Since the elastic modulus and hardness of GDC are ~ 230 GPa and ~ 14 GPa, respectively [36, 40], which are significantly higher than the values of single phase BCZ20Y15 [52], it is reasonable to assume that the mechanical response to indentation testing of the material is enhanced when a phase with higher elastic modulus and hardness exists in the composite [40, 72].

Different from the elastic modulus, the noticeably decreases when the load is increased from 200 mN to 1 N, and remains approximately constant with increasing loads. When the applied load is ≥ 1 N, the results

apparently reflect the global properties of material and the hardness decrease may result from the formation of radial/median cracks at higher loads [60].

The diameter of the micro-pillar was ~ 15 μm, which is distinctly larger than the grain size. Therefore, the micro-pillar splitting test can be used to investigate the material global mechanical properties, as reported in [73-75]. Representative load-depth curves of the BCZ20Y15-GDC15 micro-pillar splitting tests, together with the load-depth curve of indentation test on BCZ20Y15-GDC15 into the bulk region as reference are presented in Fig. 3. Furthermore, a representative load-depth curve of a single-phase BCZ20Y15 micro-pillar splitting test [52] has been added into Fig. 3.

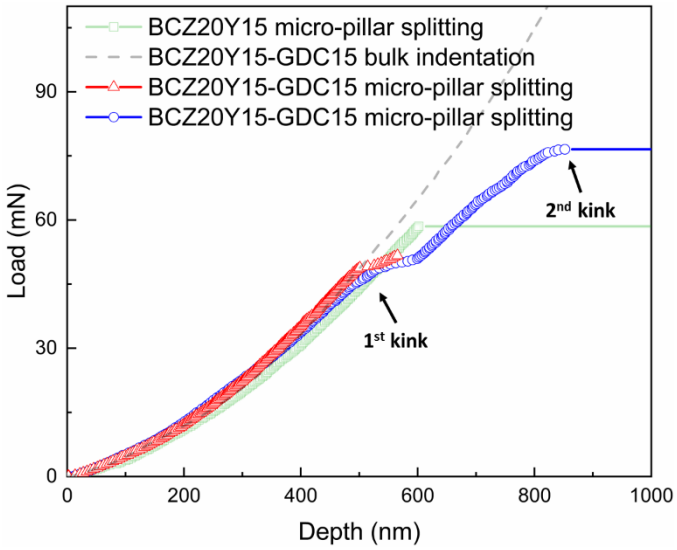

Figure 3. Representative load-depth curves obtained from the BCZ20Y15-GDC15 micro-pillar splitting tests (red and blue lines), together with the representative indentation load-depth curve on BCZ20Y15-GDC15, as reference (gray dashed line). A representative load-depth curve of a single-phase BCZ20Y15 micro-pillar (15 μm pillar size) splitting tests [52] is shown by the green symbols.

The good agreement between the dual-phase pillar splitting curves and the indent curve, obtained on the sample bulk region, confirms the validity of the results [52, 59, 62].

Obviously, two kinks are observed during the dual-phase micro-pillar splitting tests. This phenomenon has never been reported in single-phase micro-pillar splitting investigations [46, 47, 51, 52, 59, 62, 63], in which only one kink was observed, corresponding to the critical load for crack initiation [46, 47].

To clarify the origin of the two kinks, a post-test SEM characterization was performed (Fig. 4).

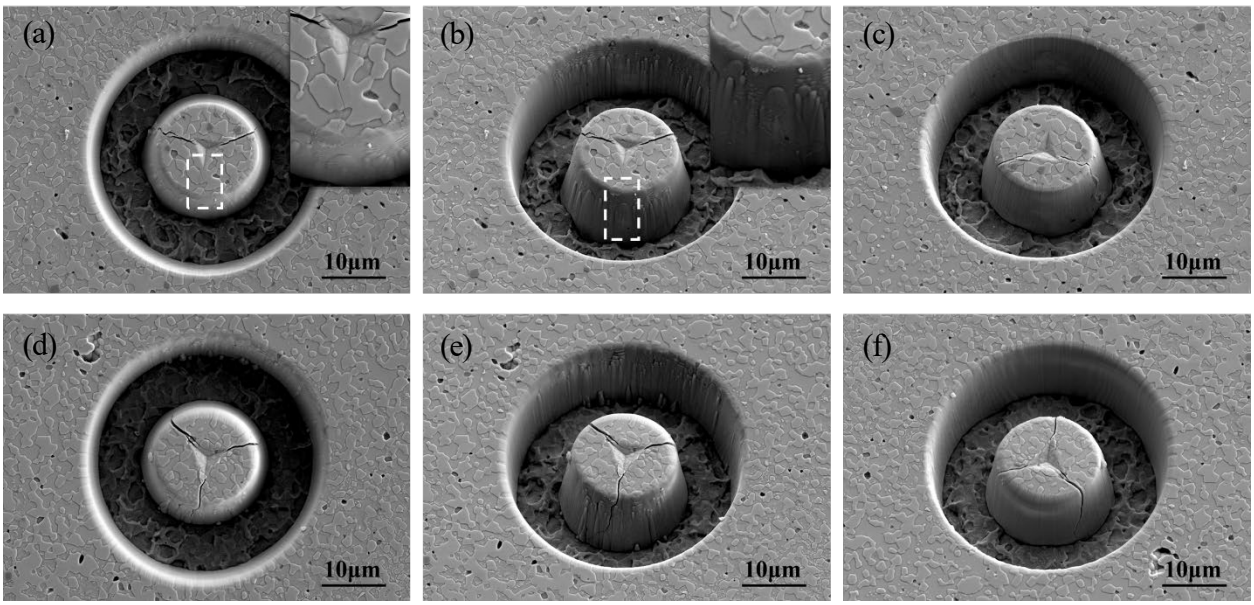

Figure 4. SEM investigation of pillars after splitting experiments: (a) Top view, (b) side view (sample tilt 26°) and (c) side view (at 180° rotation) of a pillar exhibiting only one kink in the curve. The inset in (a) shows a very thin "3rd crack", that can't be seen in the inset in (b). The other two cracks (c) reach the pillar bottom. (d) Top view, (e) side view (sample tilt 26°) and (f) side view (at 180° rotation) of a pillar with two kinks.

The indentation locations are all within pillar center 10% region, which ensures test validity and reliability of the derived K_{IC} [51]. In the top view image (Fig. 4 (a)) showing the pillar test that was terminated after the first kink (Fig. 3), only two cracks can be clearly observed. The expected 3rd crack is faintly visible in the magnified inset, but appears to be very narrow compared to the other cracks. Such a phenomenon was neither observed in our previous work [52] on single-phase BCZ20Y15, nor reported in other micro-pillar splitting investigations on single-phase materials [51, 59, 63, 76-80]. Potential reason for

this effect can be the large difference of the mechanical properties of GDC15 and BCZ20Y15 [36, 40, 52], in particular the higher fracture toughness of GDC15. An observation of the side surface (Fig. 4 (b)) reveals no trace of the 3rd crack, whereas the other two cracks (Fig. 4 (c)) could clearly be confirmed, indicating that the pillar did not split completely in this test.

After the occurrence of two kinks, the pillar (Fig. 4 (d)) shows clearly the typical, expected 3-way-split [51]. Cracks propagate on the pillar side walls (Fig. 4 (e, f)) directly down to the bottom of the pillar, similar as observed for single-phase BCZ20Y15 [52], indicating that the pillar entirely splits.

Based on the post-test observation, the "1st kink" corresponds to the pillar splitting partially, and the crack propagated mainly through BCZ20Y15 phase. The "2nd kink" corresponds to the pillar splitting completely, and during this splitting the crack proceeds through the tougher GDC15 phase. According to the classical theory developed by Lawn et al. [81], regarding the initial crack nucleation, and the FEM analysis on crack geometries of pillar by Sebastiani et al. [47], a series of FIB cuts on the selected pillars was performed to gain further insight on microstructural effects (Fig. 5).

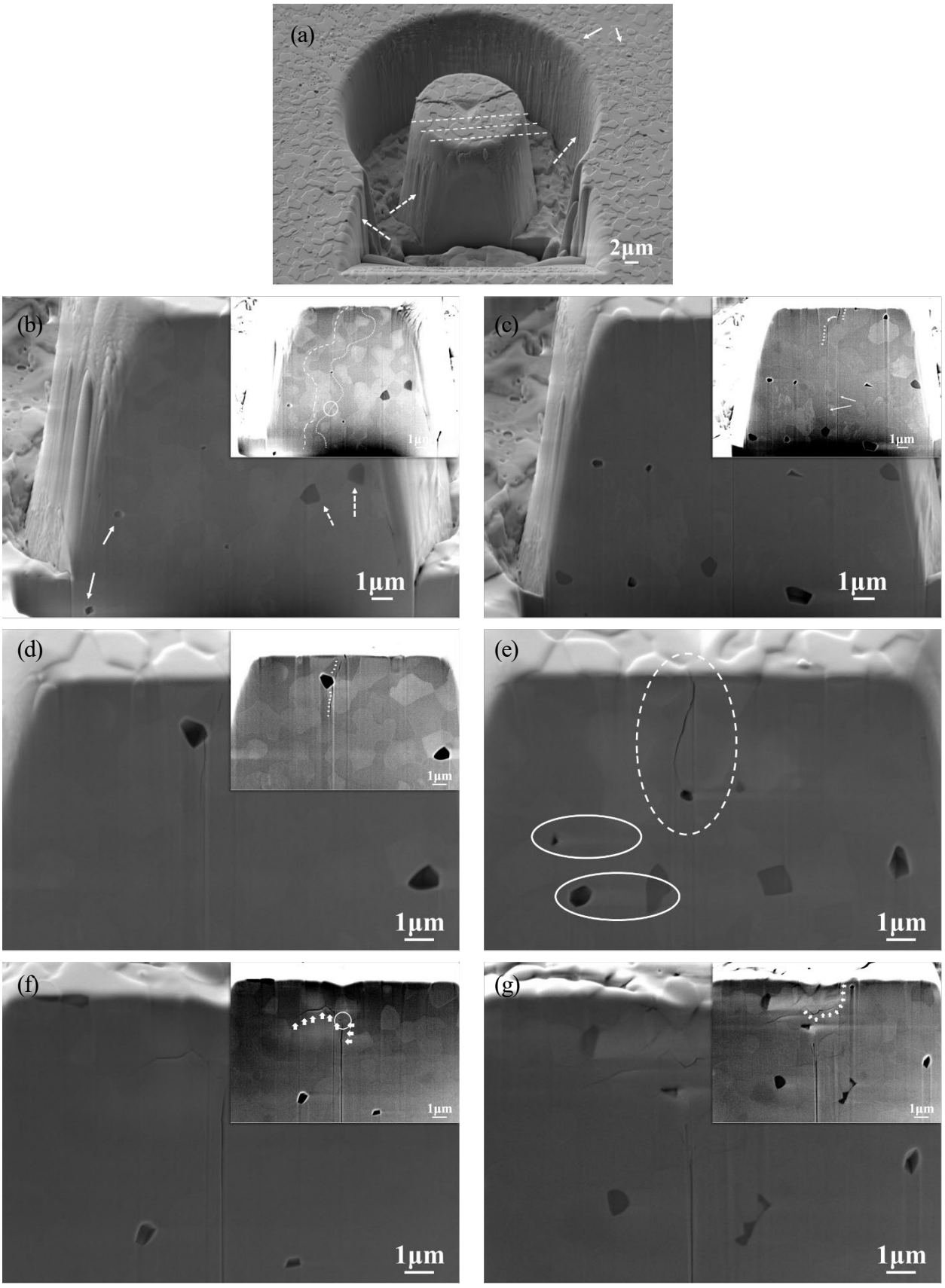
(a)
2μm
(b)
1μm
(c)
1μm
(d)
1μm
(e)
1μm
(f)
1μm
(g)
1μm

Figure 5. Slice-by-slice FIB milling of pillar with one kink. (a) Firstly, a window was milled. The solid arrows mark blister-like morphologies. The curtain artifacts, straight down to the pillar bottom, is marked by dashed arrows. Further FIB milling was performed to follow the direction of the 3rd crack, as marked by dashed lines. (b) The solid arrows indicate pores, and the dashed arrows mark Ni exsolution. The dashed and the dotted line mark the individual phases' connections of GDC15 and BCZ20Y15, respectively. The circle marked region in the line demonstrates a path although narrow but indeed connected in spatial. (c) The long arrows mark the FIB curtaining artifact. The short arrows mark that crack propagation stops at GDC15, and then continues to propagate in BCZ20Y15, as marked by the curved arrow. (d) The crack propagates through BCZ20Y15 towards pores and deflects after encountering the pores (marked by the short arrows). (e) Crack deflection due to pores (dashed circle). Fuzzy bands, marked by the solid circles, due to charging and drift. (f) The median and radial cracks are marked by short arrows. The location of the initial crack nucleation was marked by a circle. (g) The plastic zone, marked by the short arrows.

To perform the slice-by-slice FIB milling for further observation, as a first step, a window was cut (Fig. 5 (a)), see also [52, 59, 80]. The solid arrows mark some blister-like morphologies, being surface contaminations induced by the Ga^+ implanted into the materials' surface region during FIB milling. A ~ 20 - 30 nm thickness amorphous layer has been reported in case of Si [51] and Ga^+ substitution in case of $Li_7La_3Zr_2O_{12}$ [82], potentially leading to local fracture toughness increase in particular when pillar sizes are less than 10 μm [51]. These effects will be discussed below regarding Fig. S2.

In order to observe the 3rd crack inside the pillar, slice-by-slice FIB milling followed the dashed lines marked direction (Fig. 5 (a)). It should be noted that there was no trace of a 3rd crack on the sidewall, as discussed with respect to Fig. 4 (b).

The solid arrows in Fig. 5 (b) show pores inside the pillar, and the dashed arrows indicate Ni exsolution, which has been discussed above (Fig. 2 (a)). Although from the original SEM graphs different contrast can already be observed, an inset with adjusted brightness/contrast was added to highlight the sub-features, see also [52]. There is obviously a brighter phase and a darker phase. As already discussed above (Fig. 2 (a)) the

topographically higher phase corresponds to GDC15 and lower phase to BCZ20Y15, and hence it can be concluded that the brighter phase is GDC15 and the darker phase is BCZ20Y15.

The long arrows in Fig. 5 (c) mark FIB curtaining artifacts, as discussed above (Fig. 5 (a)). Crack propagation stopped in front of GDC15 and then it re-propagated in BCZ20Y15, as marked by the short arrows, indicating the existence of "crack jump" marked by the curved arrow, which can be a crack bridging effect [83] reducing the stress field, or another kind of crack deflection [84] in the 3rd dimension, which can't be observed in this cross-section.

The short arrows in Fig. 5 (d) highlight that the crack proceeds through the weaker phase (BCZ20Y15) [36, 40, 52], towards the weakest phase (pores) [85], and then deflect after encountering the pores, which is similar as reported in [86] and the crack deflection model, developed for porous ceramic interlayers, [87] can explain this behavior.

The 3rd crack indeed exists inside the pillar, as marked by the dashed circle in Fig. 5 (e), but shallow and narrow, which is consistent with the crack geometry for a "just prior to instability load" [47], indicating that the pillar's "3rd crack" side did not entirely split, which exactly confirms the above interpretation regarding Fig. 4 (b). Besides, crack deflection due to pores was observed, similar as observed in [52]. Fuzzy bands, marked by solid circles, were observed as a result of long-time under FIB and SEM leading to charging and drift.

Median and radial cracks, marked by short arrows in Fig. 5 (f), indicate a half-penny crack mode [60]. It should be noted that the marked region is indeed a median crack rather than FIB curtaining artifact, since it is deep and tilts rather than being shallow and straight down to the bottom, which can be distinguished in the original SEM graph. The initial crack nucleation, marked by the circle, is on the interface of plastic zone and elastic region, according to the classical theory developed by Lawn et al. [81].

The plastic zone, marked by the short arrows in Fig. 5 (g), is not very typical, especially when compared with what observed in the case of single phase BCZ20Y15 [52], potentially due to the large differences of GDC15 and BCZ20Y15 mechanical properties [36, 40, 52]. Besides, pores and associated charging effects lead to fuzzy bands rendering microstructural observation difficult.

Similar to the "1st kink stop" pillar, a slice-by-slice FIB milling was also performed on the selected "2nd kink stop" pillar (Fig. 6).

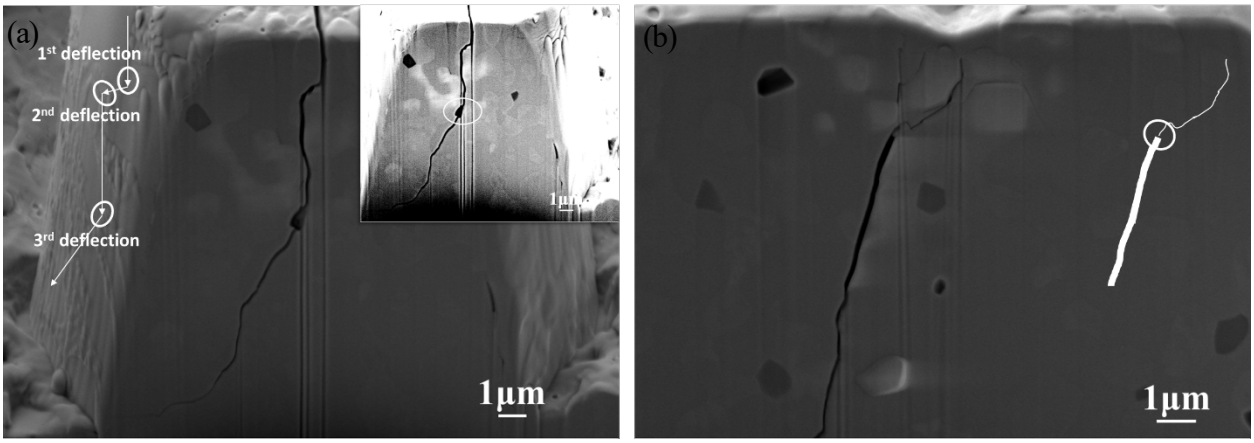

Figure 6. Slice-by-slice FIB milling of pillar with two kinks: (a) A series of crack deflections were observed. The inset at adjusted brightness/contrast shows the crack deflection. Pores, marked by the circle. (b) Thin cracks were observed inside the plastic zone, as illustrated in the sketch. The typical median crack (significantly wider). The circle marks the apparent initial crack nucleation position.

Similar as for the "1st kink stop" pillar (Fig. 5), a slice-by-slice FIB milling was conducted on the selected "2nd kink stop" pillar (Fig. 6). It's clear that the 3rd crack exists on the sidewall, similar as in [52, 59], but being different from what is observed on the "1st kink stop" pillar (Fig. 5 (a, b)), indicating that the "2nd kink stop" pillar indeed entirely split.

A series of three crack deflections were observed (Fig. 6 (a)) and from the adjusted brightness/contrast inset, it's clear that the crack deflected to avoid the GDC15 phase, due to the difference between GDC15

and BCZ20Y15 properties [36, 40, 52], similar as reported in [88], in which crack deflect or bifurcate to avoid the tougher layers. The pores, marked by the circle, apparently are responsible for the 3rd crack deflection, as also discussed above (Fig. 5 (d)).

Due to the different crack growth resistance of GDC15 and BCZ20Y15 [36, 40, 52], some narrow cracks occurred in the plastic zone (Fig. 6 (b)), as demonstrated by the sketch. Below that, a typical median crack can be seen, which is wider, similar as observed in [52]. An initial crack nucleation can be seen at their interconnection region, as marked by the circle, following Lawn's theory [81].

The above analysis on the selected "1st kink stop" pillar and "2nd kink stop" pillar verifies the former interpretation. After revealing what these two kinks represent, the microscale intrinsic fracture toughness can be derived based on Eq. 6, resulting in the values shown in Fig. 7.

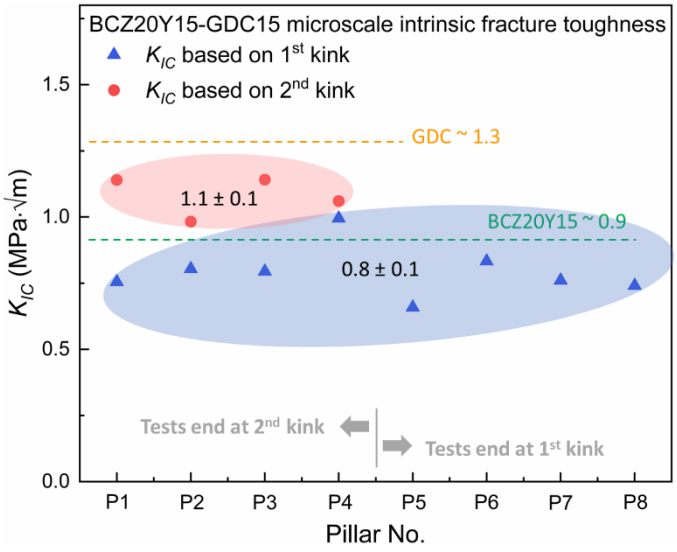

Figure 7. Microscale intrinsic fracture toughness of BCZ20Y15-GDC15 determined from pillar splitting. For Pillars P1 to P4, two kinks were observed, yielding ~ 1.1 MPa·√m evaluating the load at the 2nd kink (red circles). For pillars P5 to P8, the tests ended after the 1st kink, yielding ~ 0.8 MPa·√m (blue triangles). Reference lines for single-phase GDC10 and BCZ20Y15 are also added (~ 1.3 MPa·√m [40] and ~ 0.9 MPa·√m [52], respectively).

The pillars 1 to 4 showed curves with 2 kinks, pillars 5 to 8 only 1st kink (the grouping of the pillars with 2 kinks, i.e. 1 to 4, and the ones with 1 kink, i.e. 5 to 8, does not correspond to the order of the tests and was done after the test series to simplify the discussion). The derived 1st kink pillars lead to K_{IC} values of ~ 0.8 ± 0.1 MPa·√m, which agrees well with the single-phase BCZ20Y15 pillar splitting result [52], as marked by the green dashed line in Fig. 7. This means that the 1st kink indeed corresponds with the pillar weaker side (BCZ20Y15) split, as already discussed in Fig. 5. The derived 2nd kink corresponding K_{IC} is between the K_{IC} of single-phase BCZ20Y15 [52] and GDC10 [40], with a value of ~ 1.1 ± 0.1 MPa·√m, indicating that the 2nd kink represents a value for the whole pillar split, which is also verified in Fig. 6.

Although the pillar size is ~ 15 µm, which is significantly larger than the suggested critical pillar size to avoid the Ga^+ ion implantation effects [51], post-test EDX analysis were also performed for verification (Fig. S2).

The Ga^+ is mainly located (Fig. S2 (e)) at the edge of the pillar, similar as reported in [52, 59], implying that the indentation position is sufficiently far away from the Ga^+ affected region, which guarantees the validity of the derived K_{IC} values in Fig. 7.

A mesoscale apparent fracture toughness was also obtained via the VIF method (Fig. 8).

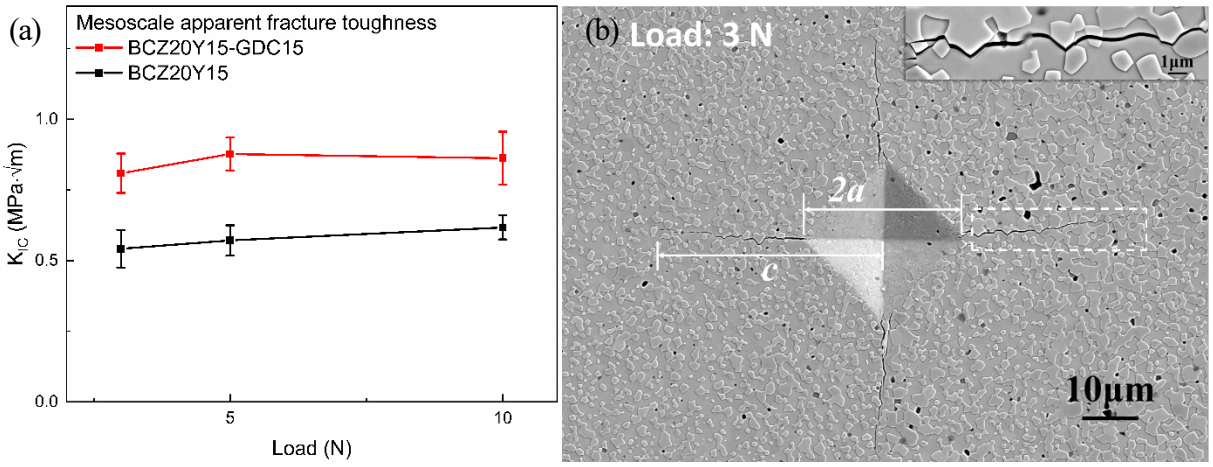

Figure 8. (a) Comparison of the Vickers indentation apparent fracture toughness values of BCZ20Y15-GDC15 and BCZ20Y15 [52]. (b) SEM observation on a 3 N Vickers imprint. The crack length *c* was used to determine the fracture toughness following the methodology outlined in [60]. The inset shows the marked region demonstrating the crack deflection to avoid GDC15.

The fracture toughness was determined from the micrographs of Vickers indentation test impressions (Fig. 8 (b)). The ratio of *c*/*a*, where *c* is the length from the indentation center point to the end of the crack tip and *a* is half of the length of the indentation impression diagonal, was confirmed to be larger than 2.5 for all loads, which usually corresponds a half-penny crack mode [60]. For the loads of 3 N, 5 N and 10 N, the fracture toughness was determined to be ~ 0.9 ± 0.1 MPa·√m (see Fig. 8 (a)), with only a negligible dependency on the applied load which is within the limits of experimental uncertainty. The mesoscale apparent fracture toughness values of BCZ20Y15-GDC15 and single-phase BCZ20Y15 [52] are presented in Fig. 8 (a). The clear difference indicates that the introduction of GDC15 indeed makes the material tougher. The reason is clearly the crack deflection, confirmed in Fig. 8 (b) inset and Fig. S3, similar as observed in Fig. 6(b). Although the validity of VIF method specifically determined values is still under discussion [45], it can still be used to permit a comparison especially for similar types of materials and crack modes, i.e. both Fig. 8 (a) and Fig. 7 indicate that BCZ20Y15-GDC15 is tougher than BCZ20Y15, on a mesoscale and microscale, respectively.

4. Conclusions

In this work, the mechanical properties of dual-phase proton conducting ceramic BCZ20Y15-GDC15 were studied using different indentation-based methods on different length scales. The elastic modulus did not depend on the applied load and was determined as ~ 170 GPa. The hardness of BCZ20Y15-GDC15 decreases with increasing indentation depth, from ~ 9 GPa at

loads lower than 200 mN to ~ 7 GPa at loads higher than 1 N, which might be due to the formation of radial/median cracks at higher loads.

The microscale intrinsic fracture toughness was determined by micropillar splitting. Slice-by-slice FIB milling of tested pillars and a detailed microstructural investigation confirmed that the 1st kink in the load-depth curve indicates the partial split of the pillar (at a lower load), while the 2nd kink corresponds the splitting of the whole pillar, as typically seen in such pillar splitting experiments. Thus, the fracture toughness of ~ 1.1 MPa·√m corresponding to 2nd kink, represents the dual-phase BCZ20Y15-GDC15 intrinsic fracture toughness. Significant toughening associated effects due to crack deflections to avoid GDC15 were observed.

The apparent fracture toughness was also estimated via the VIF method. While it represents only a rough estimate, it can still be used as a means for comparison, in particular when evaluating similar types of material. Both methods confirm that the introduction of GDC15 indeed significantly toughens the material, which can be a guide for further materials and component design.

Acknowledgements

This work was supported by the China Scholarship Council (CSC). The authors would also like to especially thank Dr. E. Wessel, Dr. D. Grüner, Mr. M. Ziegner and Ms. D. Esser for the microstructural characterization.

References

[1] K. Katahira, Y. Kohchi, T. Shimura, H. Iwahara, Protonic conduction in Zr-substituted BaCeO3, Solid State Ionics 138(1-2) (2000) 91-98.
[2] X. Ma, J. Dai, H. Zhang, D.E. Reisner, Protonic conductivity nanostructured ceramic film with improved resistance to carbon dioxide at elevated temperatures, Surface and Coatings Technology 200(5-6) (2005) 1252-1258.
[3] P. Sawant, S. Varma, B. Wani, S. Bharadwaj, Synthesis, stability and conductivity of BaCe0. 8− xZrxY0. 2O3− δ as electrolyte for proton conducting SOFC, international journal of hydrogen energy 37(4) (2012) 3848-3856.
[4] M. Yano, A. Tomita, M. Sano, T. Hibino, Recent advances in single-chamber solid oxide fuel cells: a review, Solid State Ionics 177(39-40) (2007) 3351-3359.
[5] N. Radenahmad, A. Afif, P.I. Petra, S.M. Rahman, S.-G. Eriksson, A.K. Azad, Proton-conducting electrolytes for direct methanol and direct urea fuel cells–A state-of-the-art review, Renewable and Sustainable Energy Reviews 57 (2016) 1347-1358.
[6] J. Phair, S. Badwal, Review of proton conductors for hydrogen separation, Ionics 12(2) (2006) 103-115.
[7] K. Kreuer, Proton-conducting oxides, Annual Review of Materials Research 33(1) (2003) 333-359.
[8] G. Chiodelli, L. Malavasi, C. Tealdi, S. Barison, M. Battagliarin, L. Doubova, M. Fabrizio, C. Mortalo, R. Gerbasi, Role of synthetic route on the transport properties of BaCe1− xYxO3 proton conductor, Journal of Alloys and Compounds 470(1-2) (2009) 477-485.
[9] E. Fabbri, A. D'Epifanio, E. Di Bartolomeo, S. Licoccia, E. Traversa, Tailoring the chemical stability of Ba (Ce0. 8− xZrx) Y0. 2O3− δ protonic conductors for intermediate temperature solid oxide fuel cells (IT-SOFCs), Solid State Ionics 179(15-16) (2008) 558-564.
[10] A. Magrez, T. Schober, Preparation, sintering, and water incorporation of proton conducting Ba0. 99Zr0. 8Y0. 2O3− δ: comparison between three different synthesis techniques, Solid State Ionics 175(1-4) (2004) 585-588.
[11] S. Tao, J.T. Irvine, Conductivity studies of dense yttrium-doped BaZrO3 sintered at 1325 C, Journal of Solid State Chemistry 180(12) (2007) 3493-3503.
[12] J. Li, J.-L. Luo, K.T. Chuang, A.R. Sanger, Chemical stability of Y-doped Ba (Ce, Zr) O3 perovskites in H2S-containing H2, Electrochimica Acta 53(10) (2008) 3701-3707.
[13] K.H. Ryu, S.M. Haile, Chemical stability and proton conductivity of doped BaCeO3–BaZrO3 solid solutions, Solid State Ionics 125(1-4) (1999) 355-367.
[14] S. Barison, M. Battagliarin, T. Cavallin, L. Doubova, M. Fabrizio, C. Mortalo, S. Boldrini, L. Malavasi, R. Gerbasi, High conductivity and chemical stability of BaCe 1− x− y Zr x Y y O 3− δ proton conductors prepared by a sol–gel method, Journal of Materials Chemistry 18(42) (2008) 5120-5128.
[15] S. Barison, M. Battagliarin, T. Cavallin, S. Daolio, L. Doubova, M. Fabrizio, C. Mortalo, S. Boldrini, R. Gerbasi, Barium Non‐Stoichiometry Role on the Properties of Ba1+ xCe0. 65Zr0. 20Y0. 15O3 − δ Proton Conductors for IT‐SOFCs, Fuel cells 8(5) (2008) 360-368.
[16] T. Norby, R. Haugsrud, Dense ceramic membranes for hydrogen separation, Wiley-VCH Verlag: Weinheim2006.
[17] E. Rebollo, C. Mortalo, S. Escolástico, S. Boldrini, S. Barison, J.M. Serra, M. Fabrizio, Exceptional hydrogen permeation of all-ceramic composite robust membranes based on BaCe

0.65 Zr 0.20 Y 0.15 O 3− δ and Y-or Gd-doped ceria, Energy & Environmental Science 8(12) (2015) 3675-3686.
[18] H. Kim, B. Kim, J. Lee, K. Ahn, H.-R. Kim, K.J. Yoon, B.-K. Kim, Y.W. Cho, H.-W. Lee, J.-H. Lee, Microstructural adjustment of Ni–BaCe0. 9Y0. 1O3− δ cermet membrane for improved hydrogen permeation, Ceramics International 40(3) (2014) 4117-4126.
[19] S. Fang, K.S. Brinkman, F. Chen, Hydrogen permeability and chemical stability of Ni–BaZr0. 1Ce0. 7Y0. 1Yb0. 1O3− δ membrane in concentrated H2O and CO2, Journal of membrane science 467 (2014) 85-92.
[20] Z. Zhu, W. Sun, L. Yan, W. Liu, W. Liu, Synthesis and hydrogen permeation of Ni–Ba (Zr0. 1Ce0. 7Y0. 2) O3− δ metal–ceramic asymmetric membranes, International journal of hydrogen energy 36(10) (2011) 6337-6342.
[21] S. Fang, L. Bi, C. Yang, L. Yan, C. Chen, W. Liu, H2S poisoning and regeneration of Ni–BaZr0. 1Ce0. 7Y0. 2O3− δ at intermediate temperature, Journal of alloys and compounds 475(1-2) (2009) 935-939.
[22] C. Zuo, T. Lee, S. Dorris, U. Balachandran, M. Liu, Composite Ni–Ba (Zr0. 1Ce0. 7Y0. 2) O3 membrane for hydrogen separation, Journal of Power Sources 159(2) (2006) 1291-1295.
[23] C. Zuo, S. Dorris, U. Balachandran, M. Liu, Effect of Zr-doping on the chemical stability and hydrogen permeation of the Ni− BaCe0. 8Y0. 2O3-α mixed protonic− electronic conductor, Chemistry of materials 18(19) (2006) 4647-4650.
[24] W.A. Rosensteel, S. Ricote, N.P. Sullivan, Hydrogen permeation through dense BaCe0. 8Y0. 2O3-delta-Ce0. 8Y0. 2O2-delta composite-ceramic hydrogen separation membranes, International Journal of Hydrogen Energy 41(4) (2016) 2598-2606.
[25] W.A. Rosensteel, N.P. Sullivan, Fabrication and hydrogen permeation through novel BaZr0. 9Y0. 1O3− δ–Cu composite ceramic-metallic membranes, International Journal of Hydrogen Energy 42(7) (2017) 4216-4223.
[26] Y. Wei, J. Xue, W. Fang, Y. Chen, H. Wang, J. Caro, Enhanced stability of Zr-doped Ba (CeTb) O 3− δ-Ni cermet membrane for hydrogen separation, Chemical Communications 51(58) (2015) 11619-11621.
[27] S. Escolastico, C. Solis, C. Kjølseth, J. Serra, Outstanding hydrogen permeation through CO 2-stable dual-phase ceramic membranes, Energy & Environmental Science 7(11) (2014) 3736-3746.
[28] J.M. Polfus, Z. Li, W. Xing, M.F. Sunding, J.C. Walmsley, M.-L. Fontaine, P.P. Henriksen, R. Bredesen, Chemical stability and H2 flux degradation of cercer membranes based on lanthanum tungstate and lanthanum chromite, Journal of Membrane Science 503 (2016) 42-47.
[29] J.S. Fish, S. Ricote, F. Lenrick, L.R. Wallenberg, T.C. Holgate, R. O'Hayre, N. Bonanos, Synthesis by spark plasma sintering of a novel protonic/electronic conductor composite: BaCe 0.2 Zr 0.7 Y 0.1 O 3− δ/Sr 0.95 Ti 0.9 Nb 0.1 O 3− δ (BCZY27/STN95), Journal of Materials Science 48(18) (2013) 6177-6185.
[30] D. Montaleone, E. Mercadelli, A. Gondolini, P. Pinasco, A. Sanson, On the compatibility of dual phase BaCe0. 65Zr0. 2Y0. 15O3-based membrane for hydrogen separation application, Ceramics International 43(13) (2017) 10151-10157.
[31] E. Mercadelli, D. Montaleone, A. Gondolini, P. Pinasco, A. Sanson, Tape-cast asymmetric membranes for hydrogen separation, Ceramics International 43(11) (2017) 8010-8017.
[32] C. Mortalò, E. Rebollo, S. Escolástico, S. Deambrosis, K. Haas-Santo, M. Rancan, R. Dittmeyer, L. Armelao, M. Fabrizio, Enhanced sulfur tolerance of BaCe0. 65Zr0. 20Y0. 15O3-δ-

Ce0. 85Gd0. 15O2-δ composite for hydrogen separation membranes, Journal of Membrane Science 564 (2018) 123-132.
[33] C. Mortalò, A. Santoru, C. Pistidda, E. Rebollo, M. Boaro, C. Leonelli, M. Fabrizio, Structural evolution of BaCe0. 65Zr0. 20Y0. 15O3-δ-Ce0. 85Gd0. 15O2-δ composite MPEC membrane by in-situ synchrotron XRD analyses, Materials Today Energy 13 (2019) 331-341.
[34] C. Mortalò, M. Boaro, E. Rebollo, V. Zin, E. Aneggi, M. Fabrizio, A. Trovarelli, Insights on the Interfacial Processes Involved in the Mechanical and Redox Stability of the BaCe0. 65Zr0. 20Y0. 15O3− δ–Ce0. 85Gd0. 15O2− δ Composite, ACS Applied Energy Materials 3(10) (2020) 9877-9888.
[35] F. Zeng, J. Malzbender, S. Baumann, W. Zhou, M. Ziegner, A. Nijmeijer, O. Guillon, R. Schwaiger, W.A. Meulenberg, Mechanical reliability of Ce0. 8Gd0. 2O2− δ-FeCo2O4 dual phase membranes synthesized by one-step solid-state reaction, Journal of the American Ceramic Society 104(4) (2021) 1814-1830.
[36] F. Zeng, J. Malzbender, S. Baumann, F. Schulze-Küppers, M. Krüger, A. Nijmeijer, O. Guillon, W.A. Meulenberg, Micromechanical Characterization of Ce0. 8Gd0. 2O2 - δ - FeCo2O4 Dual Phase Oxygen Transport Membranes, Advanced engineering materials 22(6) (2020) 1901558.
[37] F. Zeng, J. Malzbender, S. Baumann, A. Nijmeijer, L. Winnubst, O. Guillon, R. Schwaiger, W.A. Meulenberg, Residual stress and mechanical strength of Ce0. 8Gd0. 2O2-δ-FeCo2O4 dual phase oxygen transport membranes, Journal of the European Ceramic Society (2021).
[38] F. Zeng, J. Malzbender, S. Baumann, A. Nijmeijer, L. Winnubst, M. Ziegner, O. Guillon, R. Schwaiger, W.A. Meulenberg, Optimization of sintering conditions for improved microstructural and mechanical properties of dense Ce0. 8Gd0. 2O2-δ-FeCo2O4 oxygen transport membranes, Journal of the European Ceramic Society 41(1) (2021) 509-516.
[39] T. Nithyanantham, S. Biswas, N. Nagendra, S. Bandopadhyay, Studies on mechanical behavior of LSFT-CGO dual-phase membranes at elevated temperatures in ambient air and slightly reducing environments, Ceramics International 40(6) (2014) 7783-7790.
[40] S. Kim, S.H. Kim, K.S. Lee, J.H. Yu, Y.-H. Seong, I.S. Han, Mechanical properties of LSCF (La0. 6Sr0. 4Co0. 2Fe0. 8O3− δ)–GDC (Ce0. 9Gd0. 1O2− δ) for oxygen transport membranes, Ceramics International 43(2) (2017) 1916-1921.
[41] K. Raju, S. Kim, C.J. Hyung, J.H. Yu, Y.-H. Seong, S.-H. Kim, I.-S. Han, Optimal sintering temperature for Ce0. 9Gd0. 1O2− δ–La0. 6Sr0. 4Co0. 2Fe0. 8O3–δ composites evaluated through their microstructural, mechanical and elastic properties, Ceramics International 45(1) (2019) 1460-1463.
[42] R.O. Silva, J. Malzbender, F. Schulze-Küppers, S. Baumann, O. Guillon, Mechanical properties and lifetime predictions of dense SrTi1-xFexO3-δ (x= 0.25, 0.35, 0.5), Journal of the European Ceramic Society 37(7) (2017) 2629-2636.
[43] V. Stournari, W. Deibert, M. Ivanova, C. Krautgasser, R. Bermejo, J. Malzbender, Mechanical properties of tape casted Lanthanum Tungstate for membrane substrate application, Ceramics International 42(14) (2016) 15177-15182.
[44] L. Wang, R. Dou, G. Wang, Y. Li, M. Bai, D. Hall, Y. Chen, A case study of mechanical properties of perovskite-structured Ba0. 5Sr0. 5Co0. 8Fe0. 2O3− δ oxygen transport membrane, Journal of the European Ceramic Society 38(2) (2018) 647-653.
[45] G.D. Quinn, R.C. Bradt, On the Vickers indentation fracture toughness test, Journal of the American Ceramic Society 90(3) (2007) 673-680.

[46] M. Sebastiani, K. Johanns, E.G. Herbert, G.M. Pharr, Measurement of fracture toughness by nanoindentation methods: Recent advances and future challenges, Current Opinion in Solid State and Materials Science 19(6) (2015) 324-333.
[47] M. Sebastiani, K. Johanns, E.G. Herbert, F. Carassiti, G.M. Pharr, A novel pillar indentation splitting test for measuring fracture toughness of thin ceramic coatings, Philosophical Magazine 95(16-18) (2015) 1928-1944.
[48] M. Sebastiani, C. Eberl, E. Bemporad, G.M. Pharr, Depth-resolved residual stress analysis of thin coatings by a new FIB–DIC method, Materials Science and Engineering: A 528(27) (2011) 7901-7908.
[49] M. Sebastiani, E. Bemporad, F. Carassiti, N. Schwarzer, Residual stress measurement at the micrometer scale: Focused ion beam (FIB) milling and nanoindentation testing, Philosophical Magazine 91(7-9) (2011) 1121-1136.
[50] A. Davydok, B.N. Jaya, O. Robach, O. Ulrich, J.-S. Micha, C. Kirchlechner, Analysis of the full stress tensor in a micropillar: Ability of and difficulties arising during synchrotron based μLaue diffraction, Materials & Design 108 (2016) 68-75.
[51] C.M. Lauener, L. Petho, M. Chen, Y. Xiao, J. Michler, J.M. Wheeler, Fracture of Silicon: Influence of rate, positioning accuracy, FIB machining, and elevated temperatures on toughness measured by pillar indentation splitting, Materials & Design 142 (2018) 340-349.
[52] W. Zhou, J. Malzbender, F. Zeng, W. Deibert, O. Guillon, R. Schwaiger, W.A. Meulenberg, Mechanical properties of BaCe0. 65Zr0. 2Y0. 15O3-δ proton-conducting material determined using different nanoindentation methods, Journal of the European Ceramic Society (2020).
[53] Y.J. Kang, H.J. Park, G.M. Choi, The effect of grain size on the low-temperature electrical conductivity of doped CeO2, Solid State Ionics 179(27-32) (2008) 1602-1605.
[54] C.A. Schneider, W.S. Rasband, K.W. Eliceiri, NIH Image to ImageJ: 25 years of image analysis, Nature methods 9(7) (2012) 671-675.
[55] W.C. Oliver, G.M. Pharr, Measurement of hardness and elastic modulus by instrumented indentation: Advances in understanding and refinements to methodology, Journal of materials research 19(1) (2004) 3-20.
[56] W.C. Oliver, G.M. Pharr, An improved technique for determining hardness and elastic modulus using load and displacement sensing indentation experiments, Journal of materials research 7(6) (1992) 1564-1583.
[57] A. Atkinson, A. Selcuk, Mechanical behaviour of ceramic oxygen ion-conducting membranes, Solid State Ionics 134(1-2) (2000) 59-66.
[58] J. Gong, Determining indentation toughness by incorporating true hardness into fracture mechanics equations, Journal of the European Ceramic Society 19(8) (1999) 1585-1592.
[59] A.-N. Wang, J.F. Nonemacher, G. Yan, M. Finsterbusch, J. Malzbender, M. Krüger, Mechanical properties of the solid electrolyte Al-substituted Li7La3Zr2O12 (LLZO) by utilizing micro-pillar indentation splitting test, Journal of the European Ceramic Society 38(9) (2018) 3201-3209.
[60] C.B. Ponton, R.D. Rawlings, Vickers indentation fracture toughness test Part 1 Review of literature and formulation of standardised indentation toughness equations, Materials Science and Technology 5(9) (1989) 865-872.
[61] C. Ponton, R. Rawlings, Vickers indentation fracture toughness test Part 2 Application and critical evaluation of standardised indentation toughness equations, Materials Science and Technology 5(10) (1989) 961-976.

[62] M. Ghidelli, M. Sebastiani, K.E. Johanns, G.M. Pharr, Effects of indenter angle on micro‐scale fracture toughness measurement by pillar splitting, Journal of the American Ceramic Society 100(12) (2017) 5731-5738.
[63] A.J. Lunt, G. Mohanty, T.K. Neo, J. Michler, A.M. Korsunsky, Microscale resolution fracture toughness profiling at the zirconia-porcelain interface in dental prostheses, Micro+ Nano Materials, Devices, and Systems, International Society for Optics and Photonics, 2015, p. 96685S.
[64] M.E. Ivanova, S. Escolástico, M. Balaguer, J. Palisaitis, Y.J. Sohn, W.A. Meulenberg, O. Guillon, J. Mayer, J.M. Serra, Hydrogen separation through tailored dual phase membranes with nominal composition BaCe 0.8 Eu 0.2 O 3-δ: Ce 0.8 Y 0.2 O 2-δ at intermediate temperatures, Scientific reports 6(1) (2016) 1-14.
[65] P. Datta, P. Majewski, F. Aldinger, Synthesis and reactivity study of gadolinia doped ceria–nickel: A potential anode material for solid oxide fuel cell, Journal of alloys and compounds 455(1-2) (2008) 454-460.
[66] W. Zhou, J. Malzbender, W. Deibert, O. Guillon, R. Schwaiger, A. Nijmeijer, W.A. Meulenberg, High temperature compressive creep behavior of BaCe0. 65Zr0. 2Y0. 15O3‐δ in air and 4% H2/Ar, Journal of the American Ceramic Society (2021).
[67] X. Li, X. Xie, J. Gonzalez-Julian, J. Malzbender, R. Yang, Mechanical and oxidation behavior of textured Ti2AlC and Ti3AlC2 MAX phase materials, Journal of the European Ceramic Society 40(15) (2020) 5258-5271.
[68] X. Li, J. Gonzalez-Julian, J. Malzbender, Fabrication and mechanical performance of Ti2AlN prepared by FAST/SPS, Journal of the European Ceramic Society (2020).
[69] F. Zeng, S. Baumann, J. Malzbender, A. Nijmeijer, L. Winnubst, O. Guillon, R. Schwaiger, W.A. Meulenberg, Enhancing oxygen permeation of solid-state reactive sintered Ce0. 8Gd0. 2O2-δ-FeCo2O4 composite by optimizing the powder preparation method, Journal of Membrane Science 628 (2021) 119248.
[70] K.-D. Kreuer, S.J. Paddison, E. Spohr, M. Schuster, Transport in proton conductors for fuel-cell applications: simulations, elementary reactions, and phenomenology, Chemical reviews 104(10) (2004) 4637-4678.
[71] J. Sunarso, S. Baumann, J. Serra, W. Meulenberg, S. Liu, Y. Lin, J.D. Da Costa, Mixed ionic–electronic conducting (MIEC) ceramic-based membranes for oxygen separation, Journal of membrane science 320(1-2) (2008) 13-41.
[72] K.S. Lee, G.-H. Jo, Y.-G. Jung, Y. Byeun, Effect of carbon content on the mechanical behavior of MgO–C refractories characterized by Hertzian indentation, Ceramics International 42(8) (2016) 9955-9962.
[73] N.X. Randall, M. Vandamme, F.-J. Ulm, Nanoindentation analysis as a two-dimensional tool for mapping the mechanical properties of complex surfaces, Journal of materials research 24(3) (2009) 679-690.
[74] G. Constantinides, K.R. Chandran, F.-J. Ulm, K. Van Vliet, Grid indentation analysis of composite microstructure and mechanics: Principles and validation, Materials Science and Engineering: A 430(1-2) (2006) 189-202.
[75] L.S. de Vasconcelos, R. Xu, J. Li, K. Zhao, Grid indentation analysis of mechanical properties of composite electrodes in Li-ion batteries, Extreme Mechanics Letters 9 (2016) 495-502.
[76] M. Lilli, E. Rossi, J. Tirillò, F. Sarasini, L. Di Fausto, T. Valente, C. González, A. Fernández, C.S. Lopes, R. Moscatelli, Quantitative multi-scale characterization of single basalt

fibres: Insights into strength loss mechanisms after thermal conditioning, Materials Science and Engineering: A 797 (2020) 139963.
[77] J. Ast, M. Ghidelli, K. Durst, M. Göken, M. Sebastiani, A.M. Korsunsky, A review of experimental approaches to fracture toughness evaluation at the micro-scale, Materials & Design 173 (2019) 107762.
[78] M.Z. Mughal, H.-Y. Amanieu, R. Moscatelli, M. Sebastiani, A comparison of microscale techniques for determining fracture toughness of LiMn2O4 particles, Materials 10(4) (2017) 403.
[79] M.Z. Mughal, R. Moscatelli, H.-Y. Amanieu, M. Sebastiani, Effect of lithiation on micro-scale fracture toughness of LixMn2O4 cathode, Scripta Materialia 116 (2016) 62-66.
[80] G. Yan, J. Malzbender, S. Fu, J.P. Gross, S. Yu, R.-A. Eichel, R. Schwaiger, Fracture behavior of solid electrolyte LATP material based on micro-pillar splitting method, Journal of the European Ceramic Society 41(10) (2021) 5240-5247.
[81] B. Lawn, A. Evans, A model for crack initiation in elastic/plastic indentation fields, Journal of Materials Science 12(11) (1977) 2195-2199.
[82] L. Robben, E. Merzlyakova, P. Heitjans, T.M. Gesing, Symmetry reduction due to gallium substitution in the garnet Li6. 43 (2) Ga0. 52 (3) La2. 67 (4) Zr2O12, Acta Crystallographica Section E: Crystallographic Communications 72(3) (2016) 287-289.
[83] J. Rödel, Interaction between crack deflection and crack bridging, Journal of the European Ceramic Society 10(3) (1992) 143-150.
[84] K.T. Faber, A.G. Evans, Crack deflection processes—I. Theory, Acta metallurgica 31(4) (1983) 565-576.
[85] R.W. Rice, Porosity of ceramics: properties and applications, CRC Press1998.
[86] J.B. Davis, A. Kristoffersson, E. Carlström, W.J. Clegg, Fabrication and crack deflection in ceramic laminates with porous interlayers, Journal of the American Ceramic Society 83(10) (2000) 2369-2374.
[87] K. Blanks, A. Kristoffersson, E. Carlström, W. Clegg, Crack deflection in ceramic laminates using porous interlayers, Journal of the European Ceramic Society 18(13) (1998) 1945-1951.
[88] Y. Chang, R. Bermejo, G.L. Messing, Improved fracture behavior of alumina microstructural composites with highly textured compressive layers, Journal of the American Ceramic Society 97(11) (2014) 3643-3651.